Modal noise mitigation for high-precision spectroscopy using a photonic reformatter

F. A. Pike [1]★ A. Benoît [1] D. G. MacLachlan,[1] R. J. Harris [2] I. Gris-Sánchez [3]† D. Lee,[4] T. A. Birks[3] and R. R. Thomson[1]

[1]*SUPA, Institute of Photonics and Quantum Sciences, Heriot-Watt University, Edinburgh EH14 4AS, UK*
[2]*Zentrum für Astronomie der Universität Heidelberg, Landessternwarte, Königstuhl 12, D-69117 Heidelberg, Germany*
[3]*Centre for Photonics and Photonic Materials, Department of Physics, University of Bath, Bath BA2 7AY, UK*
[4]*STFC UK Astronomy Technology Centre, Royal Observatory, Blackford Hill, Edinburgh EH9 3HJ, UK*

ABSTRACT
Recently, we demonstrated how an astrophotonic light reformatting device, based on a multicore fibre photonic lantern and a 3D waveguide component, can be used to efficiently reformat the point spread function of a telescope to a diffraction-limited pseudo-slit. Here, we demonstrate how such a device can also efficiently mitigate modal noise – a potential source of instability in high-resolution multimode fibre-fed spectrographs. To investigate the modal noise performance of the photonic reformatter, we have used it to feed light into a bench-top near-infrared spectrograph ($R \approx 7000$, $\lambda \approx 1550$ nm). One approach to quantifying the modal noise involved the use of broad-band excitation light and a statistical analysis of how the overall measured spectrum was affected by variations in the input coupling conditions. This approach indicated that the photonic reformatter could reduce modal noise by a factor of 6 when compared to a multimode fibre with a similar number of guided modes. Another approach to quantifying the modal noise involved the use of multiple spectrally narrow lines, and an analysis of how the measured barycentres of these lines were affected by variations in the input coupling. Using this approach, the photonic reformatter was observed to suppress modal noise to the level necessary to obtain spectra with stability close to that observed when using a single mode fibre feed. These results demonstrate the potential of using photonic reformatters to enable efficient multimode spectrographs that operate at the diffraction-limit and are free of modal noise, with potential applications including radial velocity measurements of M-dwarfs.

Key words: instrumentation: spectrographs – techniques: radial velocities – planets and satellites: detection.

1 INTRODUCTION

Since the first discovery of a planet orbiting a main-sequence star in 1995 (Mayor & Queloz 1995), the search for exoplanets has been a major focus of modern astronomy. Current technology can only directly image very long-period planets using the very largest telescopes therefore detection techniques require us to look at the effect the planet has on its host star. The two most successful techniques are transit photometry (Borucki & Summers 1984), where the variation in the brightness of a star as the planet transits across it is measured, and the radial velocity (RV) method (Reiners et al. 2010), which involves measuring the Doppler shift in the host star's spectrum due to the motion around the system barycentre. When these methods are used in combination, a great deal of information can be gathered about the exoplanet in question, including the density (Charbonneau et al. 2000). Typically, an exoplanet candidate is identified using a survey telescope, which relies on transit photometry. A famous example of such a telescope is the recently retired *Kepler Space Telescope*, which has allowed the identification of more than half of all confirmed exoplanets. Among others, the recently launched *TESS* will observe the entire sky during its mission, and the PLATO mission is due for launch in 2026. They are expected to provide many new targets in the coming years. *Kepler* was designed specifically for the detection of the Earth–Sun system analogues (Koch et al. 2010), and upon analysing the data, the prevalence of terrestrial planets detected was highly encouraging, although a poor detection rate of smaller radius planets was identified (Catanzarite & Shao 2011). Following this discovery, Dressing & Charbonneau (2013) extended the *Kepler* data to smaller planets around smaller stars, and estimated that M-dwarfs hosted habitable near-Earth-sized planets at a rate of $0.15^{+0.13}_{-0.06}$ per star.

M-dwarfs are small cool stars ($\sim$2500 K) with peak blackbody emission in the near-infrared (NIR) range, and may have an anomalously high chance of hosting exoplanets. According to the study by Mulders, Pascucci & Apai (2015), there is an inverse correlation between stellar temperature and planet occurrence rates: planets around M stars occur twice as frequently as around G stars (such as

★ E-mail: fap30@hw.ac.uk
† Currently with ITEAM Research Institute, Universitat Politècnica de València, Camino de Vera s/n, 46022 Valencia, Spain (IG-S).

the Sun). Indeed, an M-dwarf hosts one of the largest Solar systems discovered to date (apart from our own) – TRAPPIST-1 (Gillon et al. 2017). The closest exoplanet to the Earth, Proxima Centauri b, also has an orbit in the habitable zone of an M-dwarf (Anglada-Escudé et al. 2016). A further advantage of performing RV measurements of these cooler, lower mass stars is the increased perturbations from habitable zone planets – the habitable zone being closer and the smaller mass disparity allows much easier detection of small rocky planets that could host life (Claudi et al. 2017).

To date, the most successful RV spectrograph is High Accuracy Radial velocity Planet Searcher (HARPS), which operates over visible wavelengths between 380 and 690 nm, with a resolving power of 115 000, and uses a multimode (MM) fibre to feed light from the telescope focal plane to the instrument, which is placed in the observatory basement where environmental conditions are strictly controlled for maximum stability (Mayor et al. 2003). Such advantages of feeding spectrographs with optical fibres are profound and well-known (Angel et al. 1977; Barden 1994). HARPS also uses a simultaneous ultrastable ThAr reference spectrum fed through an adjacent fibre, to allow an RV precision down to 30 cm s^{-1} (Fischer et al. 2016). Unfortunately, the use of silicon-based charged-coupled-device arrays in HARPS restricts its observations to visible wavelengths, preventing efficient RV measurements of M-dwarf stars whose blackbody emission peaks in the NIR. There is therefore a strong pull to develop high-precision (~ 1 m s^{-1}) spectrographs for NIR RV measurements, but this capability still remains to be addressed. To highlight the difference in precision between wavelengths, CARMENES, which saw first light in 2015, exhibits a precision of 1–2 m s^{-1} in the visible, and 5–10 m s^{-1} in the NIR (Quirrenbach et al. 2018). Roy et al. (2016) also state this discrepancy in precision goals, these being ~ 10 cm s^{-1} in the visible and < 1 m s^{-1} in the NIR. One example of a visible spectrograph with a precision goal of 10 cm s^{-1} is ESPRESSO (Pepe et al. 2010), and an example of an NIR spectrograph with a precision goal of 1 m s^{-1} is NIRPS (Blind, Conod & Wildi 2017).

The use of fibres for transporting light from the telescope focal plane to the instrument is highly advantageous for environmental stability reasons, but they are not without drawbacks. For example, modal noise (Hill, Tremblay & Kawasaki 1980; Rawson, Goodman & Norton 1980) is a phenomenon that occurs where the pattern of light at the output of the fibre evolves with time, due to fluctuations in the distribution of optical energy or relative phases of the guided modes. Modal noise will arise when the stellar image at the fibre input changes (either a change in its position as the telescope slews, or from changing atmospheric conditions), or if the fibre bends (due to the telescope slewing, thermal variations, or air currents). This drastically reduces the signal to noise (Baudrand & Walker 2001) and severely limits the accuracy of the spectrograph. A further issue with the modal noise is that it cannot be eliminated by calibration, since the injection of the calibration source will never exactly match that of the star and thus the different coupling exacerbates the modal noise.

Modal noise is obviously minimized using a single mode (SM) fibre to feed the spectrograph, but at the expense of telescope–fibre coupling efficiency, since atmospheric turbulence causes wavefront distortions and produces a stellar image that is not diffraction-limited. Extreme adaptive optics (AO) can be used to increase the coupling efficiency, and is planned for several future instruments (Crepp et al. 2016). However, this is expensive, and only possible where a suitably bright natural guide star is available, limiting the number of targets (Morris, Corrigan & Harris 2016). In any case, the point spread function (PSF) will still not be completely diffraction-limited

(Jovanovic et al. 2016). Once in the MM regime, modal noise actually reduces as the number of spatial modes increases due to statistical averaging. The number of modes (in a step index fibre), N_{modes}, is strongly dependent on the wavelength, λ, of a given fibre. This can be seen in equation (1):

$$N_{\text{modes}} = \left(\frac{\pi \cdot a \cdot NA}{\lambda} \right)^2 , \tag{1}$$

where a and NA are the fibre core radius and numerical aperture (defined by the effective core and cladding refractive indices), respectively.

The simplest approach to mitigate modal noise in MM fibre-fed spectrographs is to agitate the fibre (Baudrand & Walker 2001), which cross-couples the excited modes and averages the energy over all modes, including some that were not initially populated. This is most effectively done by hand due to the random nature of the hand movement (Plavchan et al. 2013), although an automated mechanical oscillator is more practical during observations. Other methods for mode-scrambling include using alternative fibre geometries, e.g. octagonal or rectangular core fibres (Petersburg et al. 2018). Annealed fibre has also shown effective mode-scrambling (Osterman et al. 2014) since scattering centres are produced in the fibre that distribute light uniformly both radially and azimuthally. Laser speckle reducers are also available commercially and have been used to some success by Mahadevan et al. (2014). In all of these cases, however, it is important to stress that efficient mode-scrambling becomes increasingly difficult to achieve as the number of modes decreases, making modal noise a particular challenge in precision MM fibre-fed NIR spectrographs. It is for this reason that modal noise is not a significant problem for spectrographs like HARPS that operate in the visible, but was a limiting factor in GIANO at the Telescopio Nazionale Galileo (Iuzzolino et al. 2014), which suffered from such significant modal noise that the engineers modified the entrance slit to bypass the fibre altogether (Oliva et al. 2015). This free-space approach does not take advantage of the environmental and optomechanical stability advantages offered by an optical fibre feed.

A potential alternative to standard modal-noise mitigation techniques relies on the exploitation of photonic lanterns (PLs; Leon-Saval et al. 2005; Birks et al. 2015), guided wave transitions that efficiently couple light from a MM port to an array of SM waveguides. PLs can be created in a variety of ways. For example, a multicore fibre (MCF) with a 2D array of SM cores can be heated and tapered to form an MM port when the taper is cleaved, with the taper forming a gradual transition between the MM port and the SM cores of the MCF. Such MCF–PLs are a well-suited method to eliminating modal noise in RV spectrographs (Gris-Sánchez et al. 2018; Haynes et al. 2018). A second approach involves the tapering of a bundle of SM optical fibres to form an MM port in a similar manner. Regardless of the specific fabrication approach used, a spectrograph fed with MM starlight in the form of multiple SMs should be free of modal noise. To exploit the full potential of this capability, however, it is essential to correctly arrange the SMs generated by the PL at the slit of the spectrograph, such that the individual spectra from each SM do not overlap on the detector. One approach to achieve this in MCF–PL-fed spectrographs is the TIGER method (Leon-Saval, Betters & Bland-Hawthorn 2012; Betters et al. 2020), where the MCF is rotated to the correct angle, although this technique is only applicable to systems operating in the few-mode regime. Another approach proposed by Bland-Hawthorn et al. (2010), known as the Photonic Integrated MultiMode Spectrograph (PIMMS) concept, would make the use of PLs fabricated from multiple SM fibres. In this case, the individual
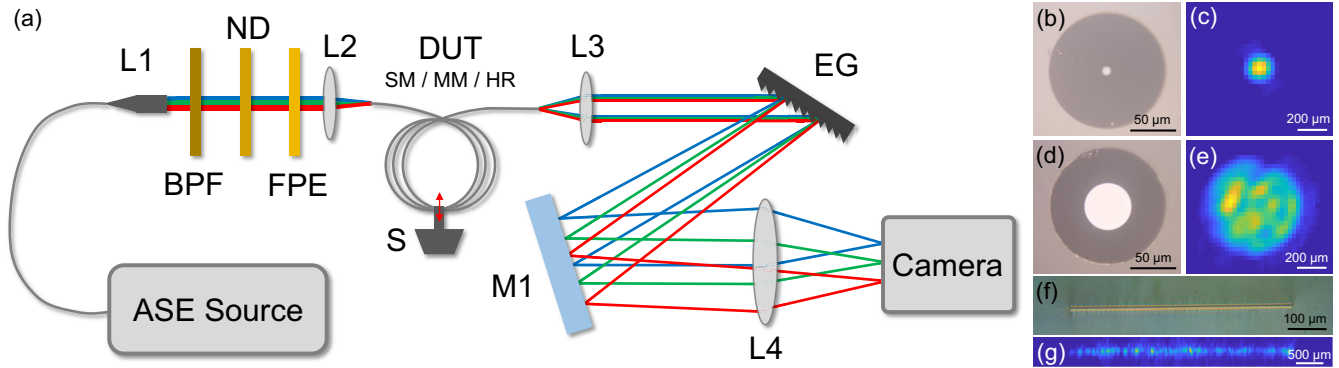
Figure 1. (a) Schematic of spectrograph layout including fibre-coupled ASE source, L1 fibre collimation package, BPF bandpass filter, ND filter, FPE Fabry-Pérot etalon (if required), L2 coupling into the device under test (DUT), mechanical shaking system S, collimation by L3, the dispersion by an Echelle grating (EG), folded by mirror M1 and focused by L4 on to an InGaAs Camera; (b) image of the 8.2 μm core SM fibre; (c) typical output light pattern of the SM fibre; (d) image of the 50 μm core MM fibre; (e) typical output light pattern of the MM fibre; (f) image of the 570 μm long pseudo-slit; (g) typical output light pattern of the single-mode pseudo-slit. Note that the image of the pseudo-slit is not to scale with the fibres, and the output light patterns are imaged through lenses that magnify the image.

SMs at the PL output can be arranged at will along the slit of the spectrograph.

Both the PIMMS and TIGER approaches can, in principle, enable very high-resolution MM spectrographs that exploit an Echelle grating (EG) for dispersion (Schwab et al. 2012; Betters et al. 2014). However, for a real spectrograph system, we ideally wish to use a single MCF–PL for capturing the telescope PSF and transporting it to a spectrograph, whilst also combining this capability with the mode-reformatting flexibility offered by PLs fabricated from individual SM fibres. As we have demonstrated previously (MacLachlan et al. 2017), one solution is the combination of an MCF–PL with a 3D integrated optical waveguide mode-reformatting component fabricated using ultrafast laser inscription (ULI) – an advanced laser manufacturing technique. We have demonstrated that this combination of technologies can be seamlessly integrated together to efficiently reformat the MM PSF of the CANARY AO system operating on the William Herschel Telescope to a SM pseudo-slit, with an on-sky throughput of 53 ± 4 per cent in the *H* band. Although the on-sky throughput results were promising, no results relating to the modal noise performance of the device were reported.

To address this, we characterized the device using a single wavelength to simulate high resolution, both experimentally and theoretically (Spaleniak et al. 2016). Initial findings suggested modal noise, whilst largely suppressed, was still present in the output of the device. This was in agreement with other experiments (Cvetojevic et al. 2017) and showed that to properly estimate the modal noise contribution from a photonic reformatter, a full characterization of the device was required.

In this paper, we use a simple NIR spectrograph to investigate in detail the modal noise performance of the photonic reformatter demonstrated on sky in MacLachlan et al. (2017), and compare its performance to SM and MM fibres. We call this device the 'hybrid' reformatter since it integrates an MCF–PL and a ULI fabricated mode reformatting component. In Section 2, we will outline the experimental design of the spectrograph and the experimental techniques used to investigate the modal noise performance. In Section 3, we describe the data processing methods and the results obtained, which demonstrate that near-SM performance can be obtained using the hybrid reformatter (HR). In Section 4, we link the precision of our device to potential scientific applications.

2 EXPERIMENTAL SPECTROGRAPH DESIGN AND DATA CAPTURE METHODS

We have designed an inexpensive bench-top spectrograph constructed from catalogue components, which enables observation and quantification of modal noise using different optical fibre feeds. For our purposes, light was fed into the spectrograph using three devices; the HR, an SMF28e fibre patch cord with FC/PC connectors at both ends, and a step index MM fibre. The SMF28e fibre exhibits a mode field diameter (MFD) of 10.4 ± 0.5 μm at 1550 nm and an NA of 0.12 based on its 0.36 per cent core-cladding refractive index contrast (Chandrasekharan et al. 2020). The MM fibre has a 50 μm core diameter and an NA of 0.22, again based on its 1.2 per cent core-cladding refractive index contrast (Thorlabs 2019). The MM input of the HR has a core diameter of 43 μm and an NA of 0.22 based on its 1.2 per cent core-cladding refractive index contrast, as specified by the manufacturer of the custom part. The pseudo-slit output exhibits a MFD of 8.5 μm at 1550 nm and a physical size of 6.7 ± 0.7 μm. Using this information, we have used BEAMPROP software to estimate the core-cladding refractive index contrast (0.65 ± 0.15 per cent), and from this we calculate the pseudo-slit exhibits an NA of 0.14 ± 0.02. All devices had a length of approximately 2 m. A schematic of the spectrograph design, images of the end-facets of the three devices, and their respective typical output light patterns are presented in Fig. 1. A schematic of the complete HR is presented in Fig. 2. It is crucial to highlight that the number of guided modes (around 124) supported in this 50 μm MM fibre at 1550 nm is reasonably close to the 92 modes processed by the HR. This MM fibre was chosen to facilitate the closest possible comparison using an off-the-shelf fibre.

For all characterization experiments, the light source used was an SM fibre-coupled broad-band amplified spontaneous emission (ASE) source (Thorlabs FL7002-C4) centred on 1560 nm with a bandwidth (measured at the −10 dB points relative to the peak) of approximately 75 nm, which is close to the centre of an M-dwarf emission spectrum. A bandpass filter (BPF; Thorlabs FB1550-12) with a full width at half-maximum (FWHM) of 12 nm was also used to ensure that the spectrum was within one free spectral range of the EG, eliminating the need for cross-dispersion. Neutral density (ND) filters were placed in the input beam path as necessary to avoid saturating the camera. Lens L1 is a 15.58 mm focal length fibre collimation package (NA 0.16) and lens L2 is a 10 mm focal length and 8 mm diameter achromatic doublet, producing an image
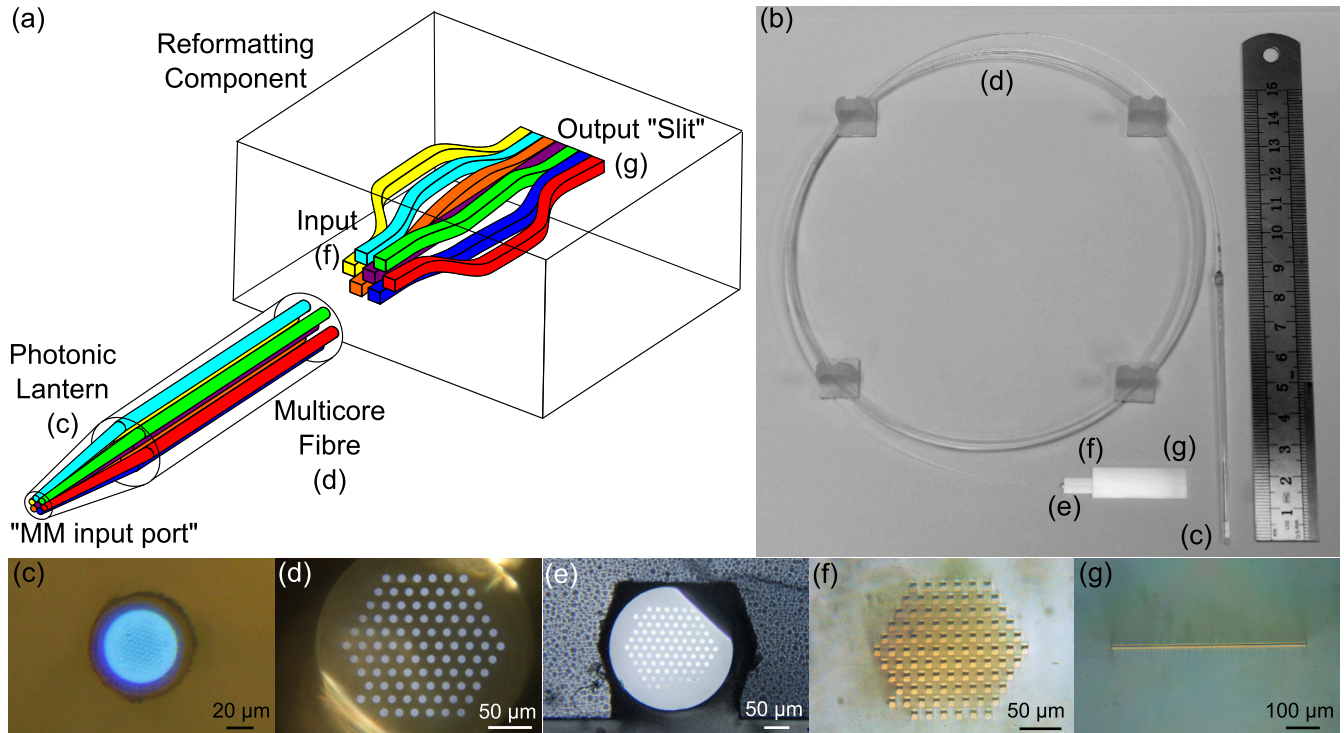
Figure 2. Key: (a) Schematic diagram of the complete device with the different colours showing the paths of the SMs, (b) Photograph of the device with 15 cm ruler for scale, (c) MM input facet of the PL, (d) MCF of 92 cores in a hexagonal array with a core-to-core pitch of 17.6 μm, (e) MCF placed in a V-groove, (f) input facet of the ULI reformatter chip, and (g) SM pseudo-slit output. From MacLachlan et al. (2017).

of the fibre mode that has an MFD of 6.7 ± 0.5 μm. This image is initially aligned with the input to the device under test (DUT) by maximizing the throughput. Lens L3 has 25.4 mm focal length, and lens L4 has 500 mm focal length for a magnification of ≈ 20. This magnification has been selected to allow the image of the pseudo-slit created by the HR to fill the majority of the detector height. The EG was sourced from Thorlabs (GE2550-0363) with 63° blaze angle and 31.6 lines mm^{-1}; this is used due to the high efficiency in higher orders, which greatly increases the dispersion and is essential to achieving a high resolution. M1 is a 2 inch square silver mirror used to fold the beam path and overcome restrictions from bulky optic mounts. This allows the grating to be used close to its design angle (the Littrow configuration). The output raw images are recorded by a Hamamatsu C10633-23 InGaAs camera, based on a detector cell of 256 × 320 pixels with a pixel size of 30 × 30 μm. The resolving power R of the spectrograph is $\lambda/\Delta\lambda$, where $\Delta\lambda$ is the FWHM of the line function. The resolving powers we calculate for each DUT are as follows: $R \approx 9500$ for SM fibre, $R \approx 3500$ for MM fibre, and $R \approx 7000$ for the HR.

To mimic the effect of the atmosphere and telescope slewing as stars are tracked across the sky, the coupling into the fibre was adjusted in a semirandom meander across the facet while maintaining a throughput greater than 80 per cent of the maximum at optimal coupling. At each fibre position, 250 frames were captured at 15 ms exposure time with the camera. These frames were then added together to produce a single detector image for that fibre position, simulating a longer and thus more relevant exposure time. The input coupling is modified successively to obtain 60 of these images, which were then processed according to Appendix A. In the following section, we discuss how the data were analysed using two different experimental protocols to quantify the modal noise when characterizing each DUT. We also investigate the effect of shaking

the DUT on the modal noise performance. To do so, a mechanical scrambling system was constructed by fixing the centres of two independently controlled loudspeakers to loops of the DUT, which is represented by S in Fig. 1(a).

3 DATA PROCESSING TECHNIQUES AND RESULTS

3.1 Characterizing modal noise from a broad-band measured spectrum

In our characterization system, modal noise manifests itself through changes in the measured spectrum as the input coupling is varied. The strength of the modal noise can therefore be determined by quantifying how the spectrum varies across the full data set. To do so, we compare the spectrum obtained from each of the 60 images to the mean spectrum across all images. A higher degree of modal noise will result in larger differences, which can then be quantified statistically. More specifically, 60 spectra were obtained by summing each processed image along the spatial axis (as described in Appendix A). Figs 3(a)–(d) illustrate examples of raw data (unprocessed images) acquired using a single input coupling position for each of the three DUTs, including examples where the MCF of the HR is either static or shaken during the exposure, and when shaken we define this as HRS. Only the data obtained using the MM fibre with shaking (MMS) is shown because the visual difference in the images taken using with and without shaking was low by eye. Figs 3(e)–(h) present spectra obtained from the raw data sets after processing, with the black line representing the average spectrum obtained across the 60 different input coupling positions, and the red line representing the spectrum out of the 60 that was most different from the average. The peak of the spectrum appears at slightly different positions on
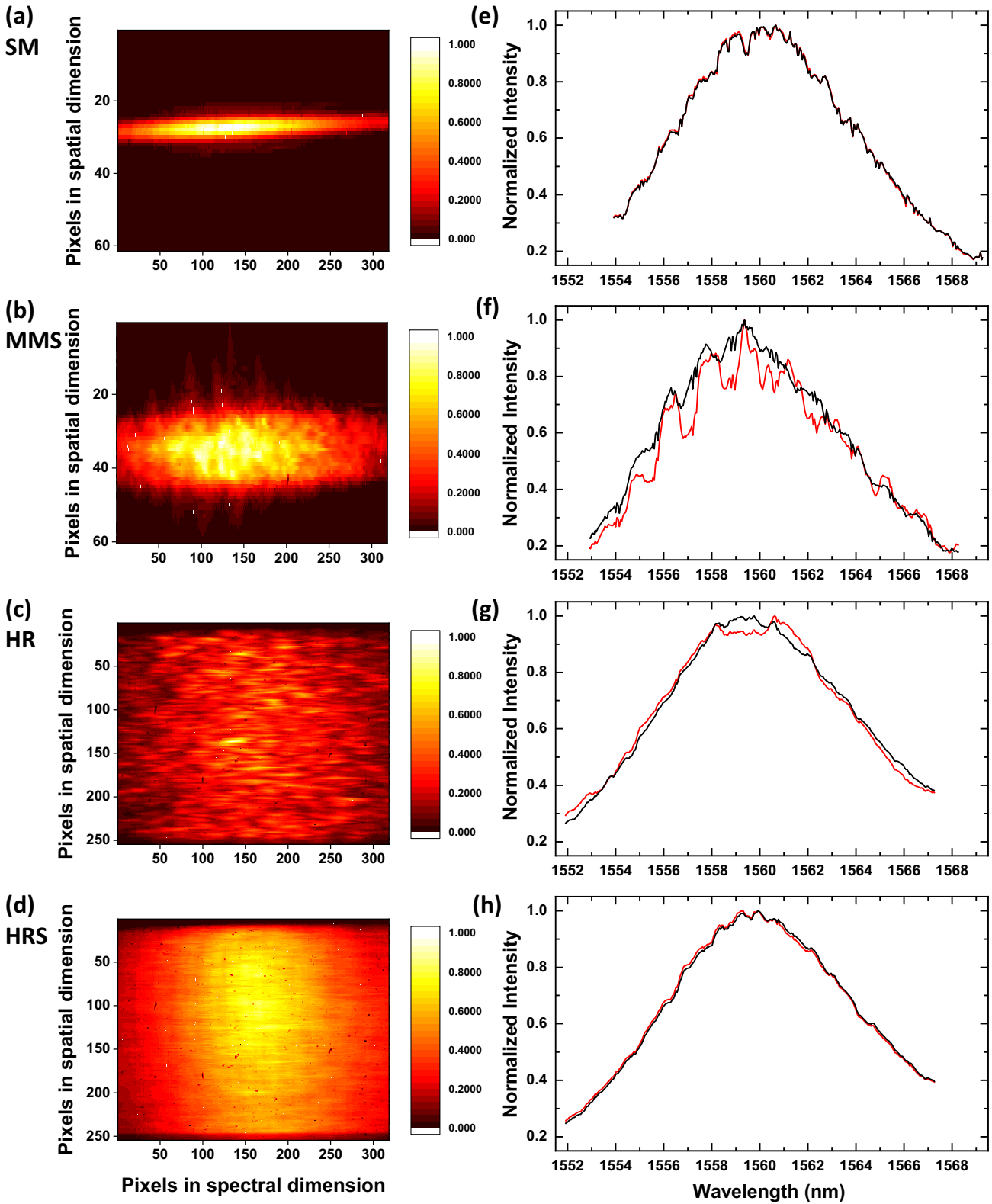
Figure 3. Examples of normalized coloured raw images for: (a) SM, (b) MMS, (c) HR and (d) HRS; Mean spectrum (the black line) and the most different spectrum (the red line) for (e) SM, (f) MMS, (g) HR, and (h) HRS. Each raw image corresponds to the most different spectrum. Some empty space on the detector with the SM and MM fibres has been omitted. Note that the normalization step shown here is shown for the benefit of the reader only, and does not form part of the data analysis in the manner depicted.
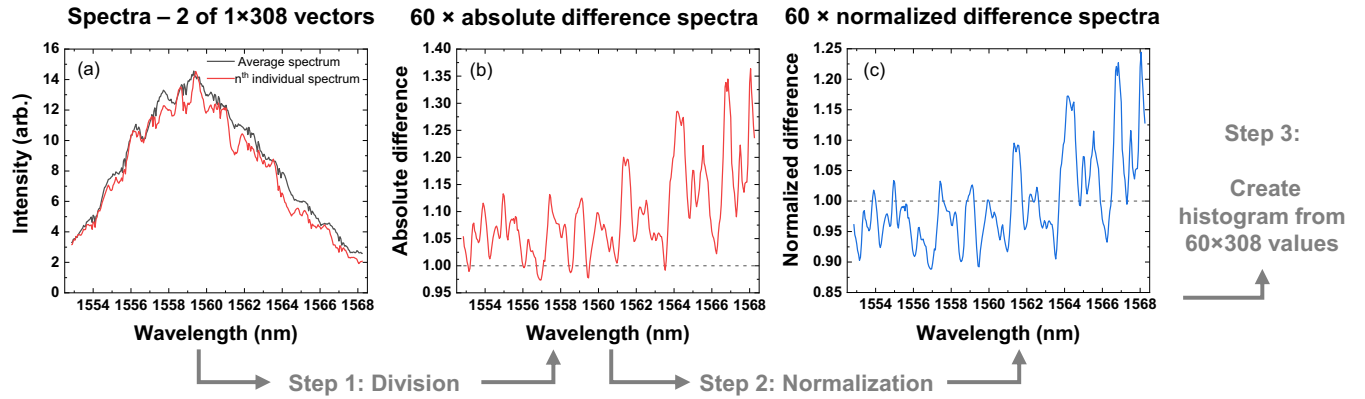
Figure 4. The three steps to obtain the histogram in Fig. 5 are illustrated using MMS data: (a) shows how the *n*th individual spectrum compares to the mean, (b) shows the absolute difference spectrum obtained by dividing these, and (c) shows the normalized difference spectrum. A histogram is then formed from the full data set of 60×308 elements.

the camera from one DUT to another due to small differences in the physical positioning of the DUT relative to the spectrograph. There is no reason to expect these differences will affect the analysis.

We provide five visualizations (available via MNRAS online - see links in 'supporting information' section) to show the effect that changing the input coupling has on the measured output, with each frame in the movie representing a different input coupling position. The difference between the data and spectra obtained using the SM fibre (Figs 3a and e) and the MMS image (Figs 3b and f) is immediately apparent. Here, we see the characteristically smooth spectrum obtained using the SM fibre, and the highly variable spectrum obtained using the MM fibre, the shape of which varies with input coupling. The difference between the spectra obtained using the HR and HRS devices is also observable, and we highlight the impact of the scrambling process in visualizations HRmov.mp4 and HRSmov.mp4. The HRS image appears very similar to the SM image spectrally, but with a large difference in the height of the area filled on the detector due to the length of the pseudo-slit. The modal noise phenomena we observe when using the HR to feed our spectrograph has some similarities to the modal noise phenomena initially observed in the RHEA instrument (Rains et al. 2016), which utilized an integral field unit with nine SM fibres. We note that the authors were also able to mitigate the modal noise in their system through fibre agitation.

The data processing steps followed to quantify the modal noise using the acquired data are depicted in Fig. 4 to aid the reader. First, by elementwise dividing the average spectrum by the nth (of 60) measured spectrum (Fig. 4a), we obtain a 308 value vector that represents the absolute deviations between the nth spectrum and average spectrum (Fig. 4b). This vector is then normalized such that the mean value is 1, which accounts for any variation in the absolute power of the nth spectrum (Fig. 4c). The deviation from unity in this vector is related to the modal noise. Once this process is applied to the full data set, a histogram of the 18 480 values, sorted into 40 bins, can be plotted to represent the spectral differences across all the 60 spectra due to modal noise. As seen in Fig. 5, the histograms (data points) that are generated by this data processing are well approximated by a Gaussian distribution, the best fit of which is also presented. We have normalized the histograms so that the Gaussian fit has a peak value of 1 to allow a straightforward comparison. The strength of the modal noise can be represented by the standard deviation (SD) of the fitted Gaussian, σ, and these can be found in Table 1, along with the goodness of fit.

Any light that is not guided within the ULI-fabricated reformatter, for example, due to coupling losses between the MCF cores and the reformatter waveguides, will significantly affect the performance of the spectrograph. To block the vast majority of this unguided light, we carefully placed opaque adhesive tape above and below the pseudo-slit at the output surface of the HR. We were also extremely careful to ensure that none of the light from the pseudo-slit itself was blocked. We have recently demonstrated how ultrafast laser microfabrication techniques can be used to create extremely precise versions of this mask (Pike et al. 2020), and such approaches will be exploited in the future to make optimal reformatting components with negligible spurious light signals.

By considering these results, it is apparent that the modal noise present in the spectra measured using the HRS is greatly reduced compared to when using either the HR or MMS devices, and is approaching the performance using the SM fibre. It should be highlighted that the width of the histogram obtained using the SM fibre represents the experimental limits of our characterization system. We see that the data obtained using the HR exhibits a factor of 2.6 reduction in modal noise compared to the data obtained with the MM device, and a factor of 2.0 reduction in modal noise compared to the data obtained using the MMS device. Shaking the MCF of the HR reduces the modal noise by a further factor of 2.9. The data obtained using MMS exhibit only a factor of 1.3 reduction in modal noise compared to the data obtained using the MM fibre. It is interesting to note that since the 9 µm diameter, 0.11 NA cores of the MCF are separated by only 17.6 µm, there will be significant intercore coupling of light along its ~2 m length. We believe that this will help to 'thermalize' the distribution of light across the modes when the HR device is shaken, and hence result in an improved modal noise performance. The total amount of modal noise mitigation is a factor of 5.7 between the HRS and the MMS – using the same scrambling system, with a small difference in number of guided modes. These results clearly demonstrate the superior scrambling ability of the HR device in comparison to the MM fibre, and demonstrates our first method to quantify how a photonic reformatter such as the HR can efficiently mitigate modal noise.

3.2 Characterizing modal noise from the barycentre precision of spectral peaks

The results outlined in Section 3.1 provide a straightforward route to quantify modal noise and modal noise mitigation, but do not
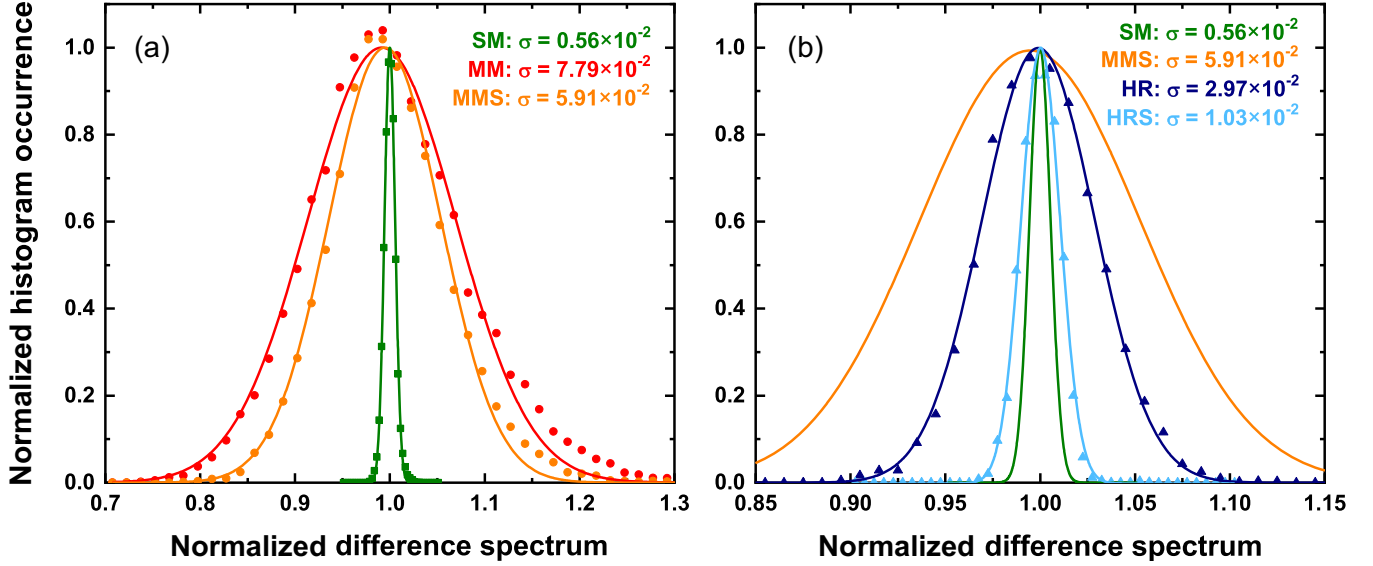
Figure 5. The data represents the histogram of the difference between spectra at different coupling positions, with a wider distribution indicating larger differences in intensity for each wavelength unit. The solid lines are a Gaussian fit to the data. (a) Normalized occurrence of difference spectrum value with changing coupling in MM (the red circles), MMS (the orange circles), and SM (the green squares) fibres; (b) Normalized occurrence of difference spectrum value with changing coupling in the HR (the dark blue triangles) and in the HRS (the light blue triangles) superimposed on to SM (the green curve) and MMS (the orange curve).

Table 1. Parameters of the fits to difference spectrum data in Fig. 5. We present σ with a factor 10^{-2} removed for ease of comparison.

Device	SD σ ($\times 10^{-2}$)	R^2 goodness of fit
SM	0.56	0.998
MM	7.8	0.989
MMS	5.9	0.995
HR	3.0	0.997
HRS	1.03	0.996

provide an immediate quantification of how modal noise affects the precision of a spectrograph. To address this, we have investigated a second method to quantify modal noise. This method uses the same characterization system shown in Fig. 1, but with a Fabry–Pérot etalon placed in the input beam path between L1 and L2, converting the smoothly varying broad-band light source into a series of discrete spectral peaks spaced by a regular frequency interval – the etalon free spectral range. As outlined previously, modal noise generates variations in the acquired spectra as the input coupling is varied. Here, we use the measured spectral stability of the etalon peaks under different input coupling conditions as a proxy for the strength of modal noise using different DUTs. The etalon we chose was sourced from Light Machinery and was made from solid fused silica with a thickness of 0.821 mm and surface reflectivities of ∼0.885 and ∼0.873, respectively. These parameters produce an etalon with a finesse of 23, generating spectral peaks with a width of approximately 40 pm spaced by ≈1 nm around 1550 nm. This etalon was chosen since the spectral peaks are sufficiently spaced such that they can still be resolved by the spectrograph when fed using light via the MM fibre. It is important to note that when using a light source with these narrow-line properties we are, in effect, observing the modal noise that would be observed using a broad-band source and a spectrograph with a resolving power (R) of ≈40 000 (1550 nm/40 pm), even though we are actually using a spectrograph

with an $R \approx 9500$ for the SM fibre feed, $R \approx 7000$ for the HR feed, and $R \approx 3500$ for the MM fibre feed.

In Figs 6(a)–(d), we present the raw images of data acquired using three DUTs (again with both unshaken and shaken conditions for the MCF of the PL). In Figs 6(e)–(h), we present how the acquired spectrum varies with input coupling, again with the solid black line indicating the average spectrum for 60 measurements, and a sample of 5 of these spectra at different coupling positions represented by the coloured dashed lines. Again, since there is a lack of visual difference between the MM fibre with and without shaking, only the MMS measurements are presented in Fig. 6. We again used the process outlined in Appendix A to correct for deviations in the straightness of the pseudo-slit and the angle between the pseudo-slit and the pixel axes of the camera.

For each of the spectral peaks generated by the etalon, a Gaussian fit was made to determine the central wavelength (barycentre). The fit was typically over 10 pixels that gave a high confidence in the precision. The variation in the acquired spectra is due to modal noise while varying the input coupling, which in turn results in variations in the measured barycentres of each peak. Thus, the SD of the 60 measured barycentres for each peak is our second measure of modal noise. These data are plotted in Figs 7(a and b), where the *x*-axis position of each data point represents the average measured barycentre for an etalon peak, and the *y*-axis position of each data point is the SD of the 60 measured barycentres for that spectral peak.

It is also useful to plot these barycentres as a ratio of the width of the peaks themselves, as this can link the precision to the resolution, plotted in Fig. 7(c). We calculate the peak width from the FWHM of the Gaussian fit. The large uncertainty for the MM/MMS measurements is due to the non-Gaussian shape of the peaks providing an imprecise fit. In Table 2, we present the mean values (and associated uncertainty from the SD of those 16 values) of the barycentre stability over each of the 16 peaks, calculated from the SD of 60 barycentres as seen in Fig. 7. It is apparent that the
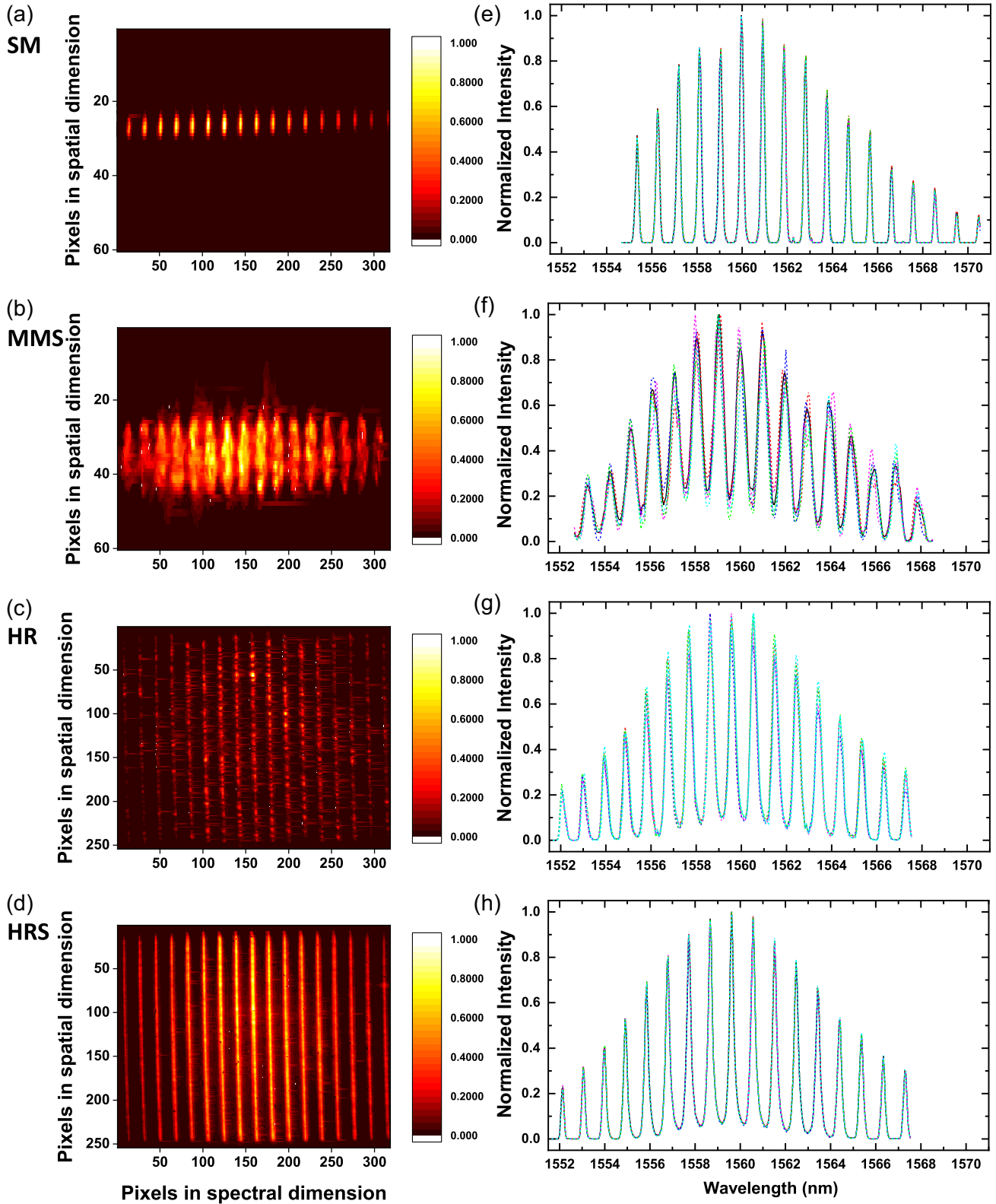
Figure 6. Examples of normalized coloured raw images with the etalon for (a) SM, (b) MMS, (c) HR, and (d) HRS; Examples of five randomly chosen spectra (the dashed line) and the mean spectrum (the solid line) for (e) SM, (f) MMS, (g) HR, and (h) HRS. Again, we present raw images of the most different spectra, and some empty space on the detector with the SM and MM fibres has been omitted.
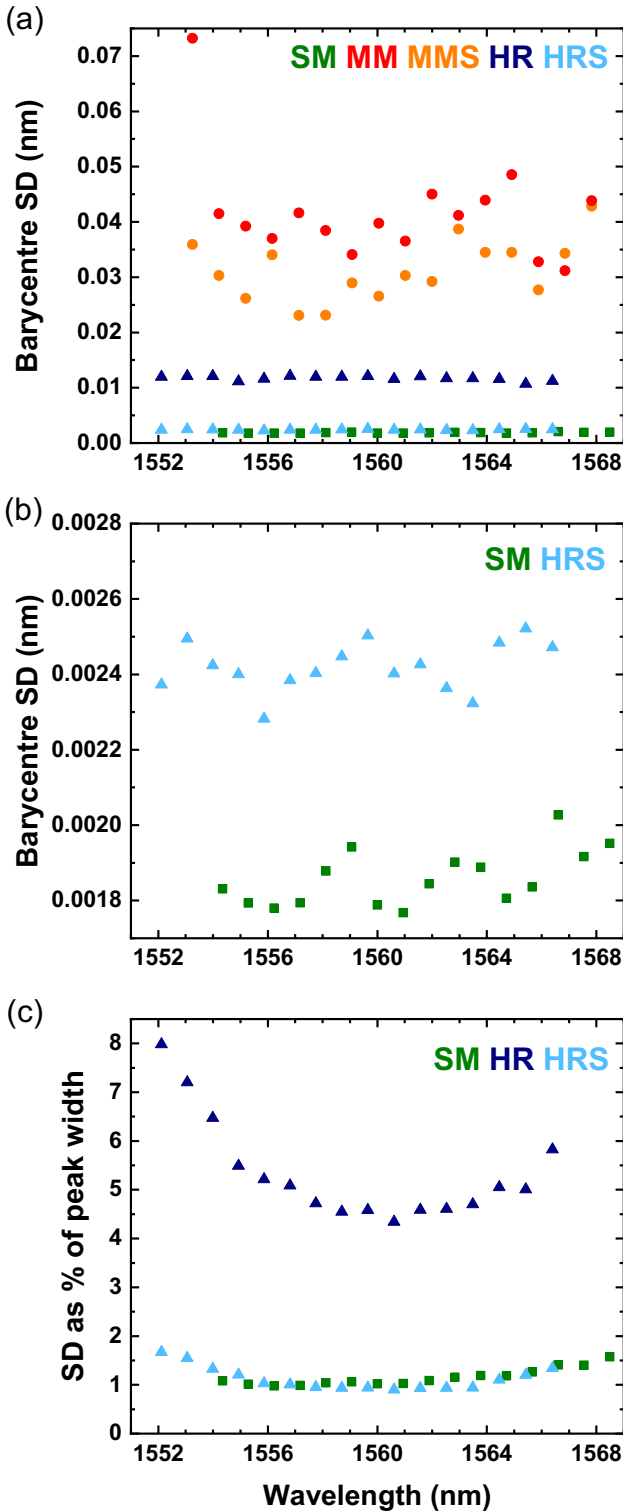
Figure 7. (a) Standard deviation of 60 calculated barycentres for each spectral peak at the given average wavelength, where the green squares correspond to SM, the red circles to MM, the orange circles to MMS, the dark blue triangles to HR, the light blue triangles to HRS; (b) Close-up of SM and HRS in (a); (c) Standard deviation of 60 calculated barycentres, plotted as a percentage of the respective peak's width, for each spectral peak at the given average wavelength. The spectra of each DUT were sampled at different positions that cause the slight offset on the graph.

Table 2. Average values of the barycentre precision presented in Fig. 7. We present the SD with a factor 10^{-3} removed for ease of comparison.

Device	Mean SD ($\times 10^{-3}$ nm)	Mean SD as per cent of peak width
SM	1.86 ± 0.07	1.2 ± 0.2
MM	42 ± 10	8 ± 2
MMS	31 ± 6	6 ± 2
HR	11.7 ± 0.4	5.3 ± 1.0
HRS	2.42 ± 0.07	1.1 ± 0.2

photonic approach using HRS offers a significant improvement over the MM fibre and a performance close to that measured using the SM fibre, and also that the mode scrambling system is highly effective – reducing the modal noise by a factor of 5 compared to when using the HR without shaking. The variation of the barycentre across the pseudo-slit with the HRS is 1.1 per cent of the peak width. The effect of shaking the MM fibre is again observed to be minimal compared to when shaking the HR. The mean SD as a percentage of the peak width for the SM fibre is equal to the HRS, showing their equivalent performance in this spectrograph.

3.3 Correcting for variations in the laboratory temperature

Our experiments were performed in a basic lab without the 0.01 K temperature control and vacuum chambers used in a state-of-the-art spectrograph. Temperature effects can therefore introduce instabilities in the spectrum that are not due to modal noise. For example, the true spectral positions of the etalon peaks may drift by 10 pm K^{-1} (Williams & Dean 2020). With the aim of accounting for the impact of laboratory thermal fluctuation on our barycentre method of quantifying modal noise, we have also conducted the following additional analysis.

It is logical to assume that laboratory temperature drifts will have a very similar effect on the spectral peaks across the measurement, since the wavelength span of the measurement is very small. Therefore, by examining the manner in which the measured spectrum shifts for each of the 60 measurements compared to the mean spectrum measured across all 60, it should be possible to substantially account and correct for laboratory temperature variations.

For a given spectrum, we use the average deviation of 15 etalon peaks from their mean positions (across the 60 measurements) as a proxy to represent how much the spectrograph has drifted from its mean position due to thermal effects – we call this shift the 'temperature proxy'. The temperature proxy was observed to gradually vary over the 60 measurements with a full range of ~8 pm. This would, for example, correspond to an etalon temperature range of slightly less than one degree. We then spectrally shift each of the 60 spectra by the temperature proxy, such that the mean position of 15 peaks is the same across all 60 measurements. This approach will compensate for variations in the laboratory temperature, leaving only the instability in the peak positions due to modal noise.

A Fourier transform of the difference spectrum between the mean spectrum in Fig. 3(h) and any one of the 60 contributing spectra indicates that the modal noise in the HRS occurs with a period that is ~25 per cent shorter than the period of the etalon peaks. Every third etalon peak therefore samples the modal noise with the same phase, meaning that the effect of the modal noise on the mean barycentre shift is negligible when considering every group of three adjacent etalon peaks. We therefore calculated the temperature proxy using the 15 etalon peaks lying closest to the
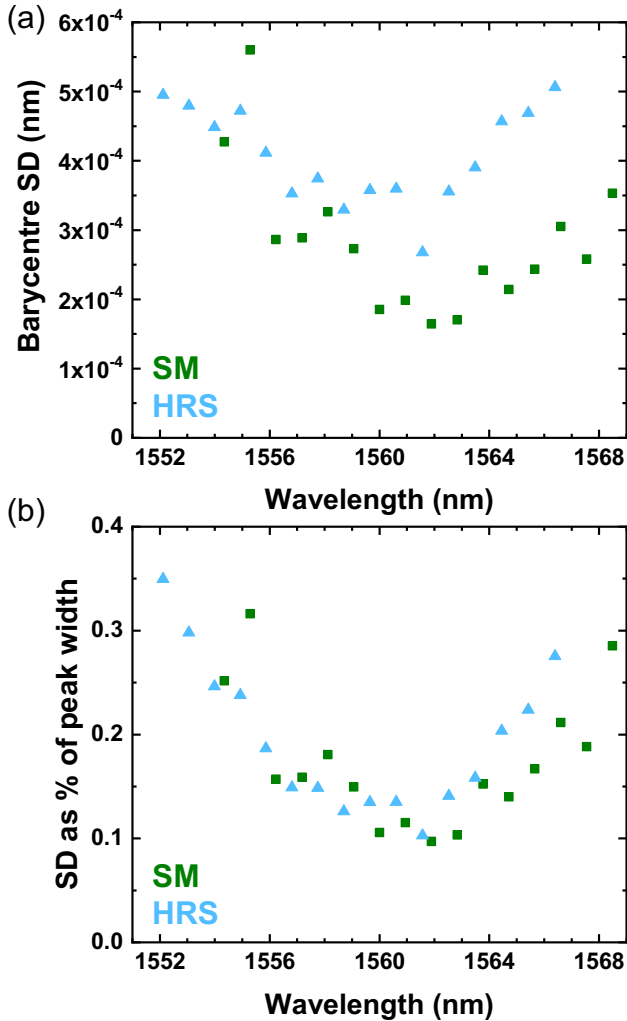
Figure 8. (a) Standard deviation of 60 calculated barycentres when laboratory temperature correction is applied to the data, for each spectral peak at the given average wavelength, where the green squares correspond to SM and the light blue triangles to HRS; (b) Standard deviation of 60 calculated barycentres when laboratory temperature correction is applied to the data, plotted as a percentage of the respective peak's width, for each spectral peak at the given average wavelength. The spectra of each DUT were sampled at different positions that cause the slight offset on the graph.

centre of the wavelength span (an integer of 3), rather than the 16 available, to minimize the potential to subtract contributions to the mean barycentre shift that are due to modal noise. To provide further confidence, we also confirmed that temperature proxy did not vary significantly when using either 14, 15, or 16 peaks to evaluate its magnitude.

The SD of the position of each of the etalon peaks relative to their respective mean positions can then be recalculated, and plotted to generate 'laboratory temperature corrected' versions of Figs 7(b) and (c), presented as Figs 8(a) and (b). In Table 3, we present the mean values of the data shown in Fig. 8. When compared to the data presented in Table 2, it is clear that accounting for the effect of laboratory temperature increases the stability of the etalon spectral peaks by a factor of ∼6 for both the SM and HRS DUTs. It is also interesting to note the shape of the curves shown in Fig. 8, where the etalon peaks are observed to be most stable in the middle of the spectral range. This, we believe, is due to the spectral peaks

Table 3. Average values of the barycentre precision presented in Fig. 8. We present σ with a factor 10^{-3} removed for ease of comparison.

Device	Mean SD ($\times 10^{-3}$ nm)	Mean SD as per cent of peak width
SM	0.28 ± 1.0	0.17 ± 0.06
HRS	0.41 ± 0.7	0.19 ± 0.07

being physically wider on the detector array in the centre of the spectral range, becoming progressively narrower to either side (the difference between the widest and narrowest peaks are factors of 1.5 and 1.9 for SM and HRS, respectively). This may be due to field curvature resulting from lens L4 that prohibits all wavelengths from simultaneously being in focus on the flat detector, and ZEMAX simulations support this belief. There is no reason to suggest that it will not be possible, with a more carefully engineered spectrograph, to achieve the stability observed with the etalon peaks in the centre of the spectral range.

Fig. 8(b) indicates that the barycentres of the etalon peaks at around 1562 nm are stable to a thousandth of the width of the peak for both the SM and HRS DUTs. Based on a barycentre precision of 8 ± 2 per cent of the peak width for the MM fibre DUT, the HRS was observed to result in a factor of 100 improvement in the barycentre stability. Anagnos et al. (2018) have used beam propagation simulations to model the propagation of light through a photonic reformatting component similar to the HR device investigated here, and concluded that they should increase the barycentre precision by a factor of 1000 compared to a 50 µm core MM fibre. It is important to note, however, that since the data we have obtained here using the SM DUT only represents the modal noise measurement limit of our characterization system and methods, Fig. 8(b) merely demonstrates that HRS exhibits a level of modal noise that is not detectable using our experimental system and the methods we have described. With an improved experimental system and optimized experimental protocol, it is logical to expect that the graphs presented in Fig. 8 will both reduce in magnitude further and eventually separate, with the data for the SM DUT dropping further.

4 COMMENTS ON ACHIEVABLE RADIAL VELOCITY PRECISION

Our study has indicated that if we were to build a temperature stabilized spectrograph fed by HRS, we would be able to achieve a barycentre stability of 0.41×10^{-3} nm. This would infer that a single spectroscopic line could be measured to an accuracy of ∼80 m s^{-1}, assuming all other sources of noise are negligible. We therefore conclude that if our spectrograph (or similar) was placed in an environmentally controlled container, it would already operate with a precision close to that required for scientific applications, e.g. for detecting hot Jupiters such as WASP-19b (Hebb et al. 2010), which orbits a star of 12th magnitude and requires a high-throughput spectrograph such as one enabled by this device. If the HRS was used to feed light into a higher resolution spectrograph (such as ≈120 000 offered by the current state-of-the-art) using a camera with smaller pixel size (15 × 15 µm is the current state of the art) we might expect the 0.1 per cent stability of HRS barycentre relative to the physical peak width to result in a single line RV precision around 1 m s^{-1}, again assuming all other sources of noise (e.g. increased role of detector noise due to the length of the slit) are negligible. This is easily low enough to detect a terrestrial exoplanet in the habitable zone around an

M-dwarf. We also note the fact that real RV measurements are almost always made by cross-correlating full spectra consisting of many spectral lines, and so it is reasonable to conclude that the achievable precision when limited by modal noise could be significantly higher.

5 CONCLUSIONS

We have developed a bench top NIR spectrograph to characterize the modal noise performance of a photonic reformatter called the HR that reformats a telescope PSF to a diffraction-limited pseudo-slit. We used the spectrograph to compare the modal noise performance of the HR to that exhibited by two reference devices: a single-mode fibre and a MM fibre that supported a similar number of guided modes. We also investigated the effect of mechanical shaking on the modal noise.

We used two methods to quantify the strength of the modal noise. In the first, we used a spectrally smooth broad-band source and a statistical analysis to quantify how the entire acquired spectrum changed as a result of different input coupling conditions to simulate the effect of telescope slewing and tracking during an exposure. Using this method, we observed that the modal noise performance of the HR when shaken was a factor of $\approx$6 better than that observed using the MM fibre when shaken, but a factor of $\approx$2 worse than when using the SM.

In the second, we used a broad-band source consisting of multiple spectrally narrow peaks to quantify how the barycentres of the peaks shift as a result of different input coupling conditions. In this case, we observed that the modal noise performance of the HR when shaken was identical to that of the SM, but we again highlight that this merely indicates that the HR when shaken exhibits a level of modal noise that is not detectable using our experimental system and the barycentre method we have described.

Finally, looking forward to science applications, we have considered the relevance of our modal noise characterization tests in the context of NIR RV measurements, concluding that HR devices could offer a powerful route to combine high throughput efficiencies enabled by multimode operation with high precision spectroscopy through strong modal noise mitigation.

ACKNOWLEDGEMENTS

DATA AVAILABILITY

The raw data is available on Heriot-Watt University's Pure data repository (Pike & MacLachlan 2020).

REFERENCES

Anagnos Th. et al., 2018, MNRAS, 478, 4881
Angel J. R. P., Adams M. T., Boroson T. A., Moore R. L., 1977, ApJ, 218, 776
Anglada-Escudé G. et al., 2016, Nature, 536, 437
Barden S. C., 1994, in Pyper D. M, Angione R. J., eds, Proc. ASP Conf. Ser. Vol. 55, Optical Astronomy from the Earth and Moon. Astron. Soc. Pac., San Francisco, p. 130
Baudrand J., Walker G. A. H., 2001, PASP, 113, 851
Betters C. H., Leon-Saval S. G., Bland-Hawthorn J., Richards S. N., Birks T. A., Gris-Sánchez I., 2014, in Ramsay S. K., McLean I. S., Takami H., eds, Proc. SPIE Conf. Ser. Vol. 9147, Ground-Based and Airborne Instrumentation for Astronomy V. SPIE, Bellingham, p. 91471I
Betters C. H., Bland-Hawthorn J., Sukkarieh S., Gris-Sánchez I., Leon-Saval S. G., 2020, IEEE Photonics Technol. Lett., 32, 7
Birks T. A., Gris-Sánchez I., Yerolatsitis S., Leon-Saval S. G., Thomson R. R., 2015, Adv. Opt. Photonics, 7, 107
Bland-Hawthorn J. et al., 2010, in McLean I. S., Ramsay S. K., Takami H., eds, Proc. SPIE Conf. Ser. Vol. 7735, Ground-Based and Airborne Instrumentation for Astronomy III. SPIE, Bellingham, p. 77350N
Blind N., Conod U., Wildi F., 2017, Presentation at 'Adaptive Optics for Extremely Large Telescopes 5 (AO4ELT5)', Tenerife, Canary Islands, Spain, June 25–30, 2017. Available at: http://research.iac.es/congreso/AO4ELT5/media/proceedings/proceeding-094.pdf (accessed January 15, 2020)
Borucki W. J, Summers A. L., 1984, Icarus, 58, 1
Catanzarite J., Shao M., 2011, ApJ, 738, 151
Chandrasekharan H. K., Ehrlich K., Tanner M. G., Haynes D. M., Mukherjee S., Birks T. A., Thomson R. R., 2020, APL Photonics, 5, 061303
Charbonneau D., Brown T. M., Latham D. W., Mayor M., 2000, ApJ, 529, 45
Claudi R. et al., 2017, Eur. Phys. J. Plus, 132, 364
Crepp J. R. et al., 2016, in Evans C. J., Simard L., Katami H., eds, Proc. SPIE Conf. Ser. Vol. 9908, Ground-based and Airborne Instrumentation for Astronomy VI. SPIE, Bellingham, p. 990819
Cvetojevic N. et al., 2017, Optics Exp., 25, 21
Dressing C. D., Charbonneau D., 2013, ApJ, 767, 95
Fischer D. A. et al., 2016, PASP, 128, 066001
Gillon M. et al., 2017, Nature, 542, 23
Gris-Sánchez I., Haynes D. M., Ehrlich K., Haynes R., Birks T. A., 2018, MNRAS, 475, 3
Haynes D. M., Gris-Sánchez I., Birks T. A., Haynes R., 2018, in Navarro R., Geyl R., eds, Proc. SPIE Conf. Ser. Vol. 10706, Advances in Optical and Mechanical Technologies for Telescopes and Instrumentation III. SPIE, Bellingham, p. 1070665
Hebb L. et al., 2010, ApJ, 708, 224
Hill K. O., Tremblay Y., Kawasaki B. S., 1980, Opt. Lett., 5, 6
Iuzzolino M., Tozzi A., Sanna N., Zangrilli L., Oliva E., 2014, in Ramsay S. K., McLean I. S., Takami H., eds, Proc. SPIE Conf. Ser. Vol. 9147, Ground-based and Airborne Instrumentation for Astronomy V. SPIE, Bellingham, p. 914766
Jovanovic N. et al., 2016, in Evans C. J., Simard L., Katami H., eds, Proc. SPIE Conf. Ser. Vol. 9908, Ground-based and Airborne Instrumentation for Astronomy VI. SPIE, Bellingham, p. 99080R
Koch D. G. et al., 2010, ApJ, 713, 79
Leon-Saval S. G., Birks T. A., Bland-Hawthorn J., Englund M., 2005, Opt. Lett., 30, 2545
Leon-Saval S. G., Betters C. H., Bland-Hawthorn J., 2012, in Navarro R., Cunningham C. R., Prieto E., eds, Proc. SPIE Conf. Ser. Vol. 8450, Modern Technologies in Space- and Ground-based Telescopes and Instrumentation II. SPIE, Bellingham, p. 84501K
MacLachlan D. G. et al., 2017, MNRAS, 464, 4950
Mahadevan S., Halverson S., Ramsey L., Venditti N., 2014, ApJ, 786, 1
Mayor M., Queloz D., 1995, Nature, 378, 355
Mayor M. et al., 2003, The Messenger, 114, 20
Morris T. J., Corrigan M., Harris R. J., 2016, in presentation at 'CLEO: Applications and Technology 2016', California, United States, June 5-10, 2016. Available at: https://doi.org/10.1364/CLEO_AT.2016.JF2N.2 (accessed January 7, 2020)
Mulders G. D., Pascucci I., Apai D., 2015, ApJ, 798, 112

Oliva E. et al., 2015, A&A, 581, A47

Osterman S. N., Ycas G. G., Donaldson C. L., Diddams S. A., Mahadevan S., Ramsey L. W., Plavchan P. P., 2014, in Ramsay S. K., McLean I. S., Takami H., eds, Proc. SPIE Conf. Ser. Vol. 9147, Ground-based and Airborne Instrumentation for Astronomy V. SPIE, Bellingham, p. 91475C

Pepe F. A. et al., 2010, in McLean I. S., Ramsay S. K., Takami H., eds, Proc. SPIE Conf. Ser. Vol. 7735, Ground-Based and Airborne Instrumentation for Astronomy III. SPIE, Bellingham, p. 77350F

Petersburg R. R., McCracken T. M., Eggerman D., Jurgenson C. A., Sawyer D., Szymkowiak A. E., Fischer D. A., 2018, ApJ, 853, 2

Pike F. A., MacLachlan D. G., 2020, in Modal noise mitigation for high-precision spectroscopy using a photonic reformatter - support data. Heriot-Watt University

Pike F. A. et al., 2020, Proc. SPIE Conf. Ser. Vol. 11451, Advances in Optical and Mechanical Technologies for Telescopes and Instrumentation IV. SPIE, Bellingham, p. 11451

Plavchan P. P. et al., 2013, in Shaklan S., ed., Proc. SPIE Conf. Ser. Vol. 8864, Techniques and Instrumentation for Detection of Exoplanets VI. SPIE, Bellingham, p. 88640G

Quirrenbach A. et al., 2018, in Evans C. J., Simard L., Takami H., eds, Proc. SPIE Conf. Ser. Vol. 10702, Ground-Based and Airborne Instrumentation for Astronomy VII. SPIE, Bellingham, p. 107020W

Rains A. D. et al., 2016, in Evans C. J., Simard L., Katami H., eds, Proc. SPIE Conf. Ser. Vol. 9908, Ground-based and Airborne Instrumentation for Astronomy VI. SPIE, Bellingham, p. 990876

Rawson E. G., Goodman J. W., Norton R. E., 1980, J. Opt. Soc. Am., 70, 8

Reiners A., Bean J. L., Huber K. F., Dreizler S., Seifahrt A., Czesla S., 2010, ApJ, 710, 432

Roy A., Chakraborty A., Mahadevan S., Chaturvedi P., Prasad N. J. S. S. V., Shah V., Pathan F. M., Anandarao B. G., 2016, in Evans C. J., Simard L., Katami H., eds, Proc. SPIE Conf. Ser. Vol. 9908, Ground-based and Airborne Instrumentation for Astronomy VI. SPIE, Bellingham, p. 99086R

Schwab C., Leon-Saval S. G., Betters C. H., Bland-Hawthorn J., Mahadevan S., 2012, in Haghighipour N., ed., Proc. IAU Symp. 293, Formation, Detection, and Characterization of Extrasolar Habitable Planets. Kluwer, Dordrecht. p. 403

Spaleniak I. et al., 2016, in Navarro R., Burge J. H., eds, Proc SPIE Conf. Ser. Vol. 9912, Advances in Optical and Mechanical Technologies for Telescopes and Instrumentation II. SPIE, Bellingham, p. 991228

Thorlabs specification sheet for part FG050LGA, 2019, web page. Available at: https://www.thorlabs.com/drawings/439e7b5e20ecea9d-8DF19B3E-9FF3-64AB-87AC4C45BF085F0B/M42L02-AutoCADPDF.pdf (accessed June 2, 2020)

Williams E., Dean J., 2020, LightMachinery Inc., web page. Available at: https://lightmachinery.com/optical-design-center/more-optical-design-tools/etalon-tuning/ (accessed January 10, 2020)

SUPPORTING INFORMATION

Supplementary data are available at *MNRAS* online.

HRmov.mp4
HRSmov.mp4
MMmov.mp4
MMSmov.mp4
SMmov.mp4

Please note: Oxford University Press is not responsible for the content or functionality of any supporting materials supplied by the authors.

Any queries (other than missing material) should be directed to the corresponding author for the article.

APPENDIX A: PROCESS TO CREATE SPECTRA FROM RAW DATA

After gathering the 60 images, some initial data processing was performed. The five hot pixels identified on the camera were all set to zero, and the outermost rows and columns of the camera images were removed from the data as they did not register any light, which results in a matrix of 254×318 elements. Additionally, there is a small but non-trivial angle between the peaks formed by the etalon when the pseudo-slit is imaged on the detector, and the spatial axes of the camera; this is most easily noticeable in Fig. 6(d). The process to 'straighten' the image is explained here with the aid of a schematic in Fig. A1. A calibration file was determined from the data gathered using the HRS, since this is more reliable than the non-shaken conditions. Starting with one image of 250 rows (we eliminate the top four empty rows to achieve a multiple of 10; Step 1), we obtain a partial spectrum for each block of 10 rows in an image (summed along the axis orthogonal to the dispersion), which we can compare to the 250-row spectrum (Step 2). We perform a cross-correlation of the two spectra, and the lag corresponding to the peak of the cross-correlation is where they show most similarity (Step 3). We did this using summed sections of 10 rows because a cross-correlation using individual rows was prone to error. Applied to the full data set, this lag, corresponding to the mth block of rows in the nth image, was set as element (m,n) in a 25×60 matrix (Step 4). This calibration matrix was then averaged down the 60 columns and rounded to an integer to determine how much each block of rows should be shifted (Step 5). The range of the shift required was ~ 7 pixels over the full length of the pseudo-slit. The calibration file was applied consistently to all 60 images in both the shaken and unshaken data sets. The resolution increased by 50 per cent – becoming more comparable to the resolution of the spectrograph when fed with SM fibre. The 'straightened' images were then summed down the spatial axis to create 60 spectra as before. This process was not used to correct the data from the SM fibre as the small angle and minimal number of rows spatially occupied by the image made the process needless. In addition to this reason being applicable to the MM fibre (albeit to a lesser extent), the modal noise present meant this method of cross-correlation was unreliable and actually decreased the resolution. In this case, it would also not be reasonable to use the same calibration file as for the pseudo-slit because the spectrograph needed some small physical adjustments to accommodate the differently shaped outputs. The calibration file was retrospectively applied to the broad-band images of the pseudo-slit without the etalon to ensure the statistical analysis we perform in section 3.1 used the spectrograph at the same resolution. The wrapping of rows when shifted caused some errors on the edges of the images, so the outer five columns on each side were truncated to ensure no unnecessary errors in the spectra were introduced by the data processing. For each DUT, to determine the relationship between pixel number and wavelength a tuneable laser (Anritsu MG9638A) was scanned across the detector in 1 nm increments. A straight line fit then gave the conversion factor (since the small wavelength range does not introduce non-linear dispersion).
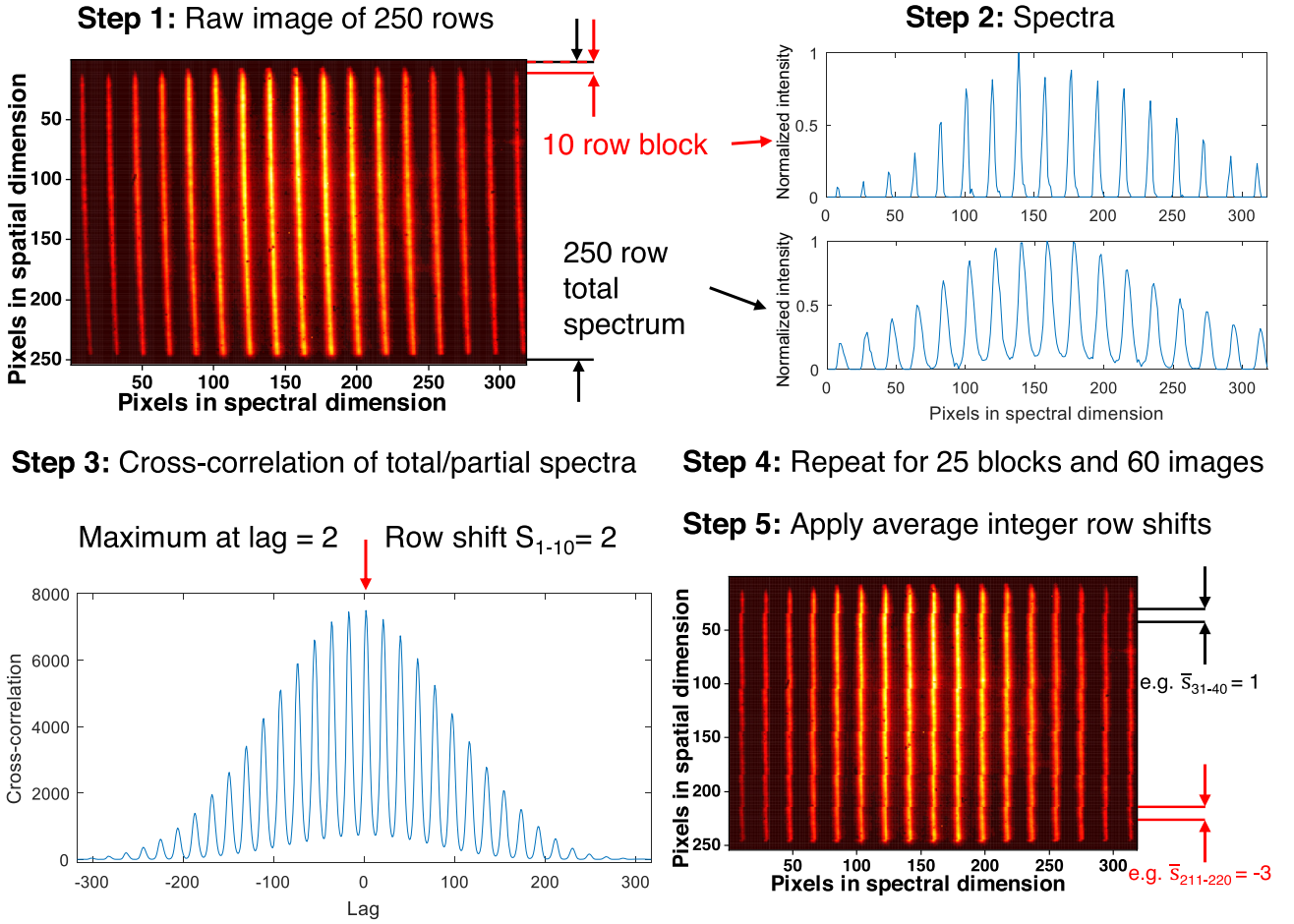
Step 1: Raw image of 250 rows

Step 2: Spectra

10 row block

250 row total spectrum

Step 3: Cross-correlation of total/partial spectra

Maximum at lag = 2   Row shift S_{1-10} = 2

Step 4: Repeat for 25 blocks and 60 images

Step 5: Apply average integer row shifts

e.g. $\bar{s}_{31-40} = 1$

e.g. $\bar{s}_{211-220} = -3$

Figure A1. The five steps to straighten the image of the pseudo-slit on the detector are presented. Step 1 is to select a raw image of 250 rows. Step 2 is to generate the total spectrum and a partial spectrum from a 10 row block. Step 3 is to perform a cross-correlation between these spectra. The lag corresponding to the maximum value is the row shift for that block and particular image. Step 4 is to repeat this for 25 blocks and 60 images to generate a matrix. The average row shift for each block is calculated and rounded to the nearest integer. Step 5 is to apply the row shifts for each block consistently for all images.

This paper has been typeset from a TEX/LATEX file prepared by the author.